

2019

# Quantitative stratigraphic analysis in a source-to-sink numerical framework

Xuesong Ding  
*University of Sydney*

Tristan Salles  
*University of Sydney*

Nicolas Flament  
*University of Wollongong, nflament@uow.edu.au*

Patrice F. Rey  
*University of Sydney*

---

## Publication Details

Ding, X., Salles, T., Flament, N. & Rey, P. (2019). Quantitative stratigraphic analysis in a source-to-sink numerical framework. *Geoscientific Model Development*, 12 (6), 2571-2585.

---

# Quantitative stratigraphic analysis in a source-to-sink numerical framework

## Abstract

The sedimentary architecture at continental margins reflects the interplay between the rate of change of accommodation creation ( $\delta A$ ) and the rate of change of sediment supply ( $\delta S$ ). Stratigraphic interpretation increasingly focuses on understanding the link between deposition patterns and changes in  $\delta A = \delta S$ , with an attempt to reconstruct the contributing factors. Here, we use the landscape modelling code pyBadlands to (1) investigate the development of stratigraphic sequences in a source-to-sink context; (2) assess the respective performance of two well-established stratigraphic interpretation techniques: the trajectory analysis method and the accommodation succession method; and (3) propose quantitative stratigraphic interpretations based on those two techniques. In contrast to most stratigraphic forward models (SFMs), pyBadlands provides self-consistent sediment supply to basin margins as it simulates erosion, sediment transport and deposition in a source-to-sink context. We present a generic case of landscape evolution that takes into account periodic sea level variations and passive margin thermal subsidence over 30 million years, under uniform rainfall. A set of post-processing tools are provided to analyse the predicted stratigraphic architecture. We first reconstruct the temporal evolution of the depositional cycles and identify key stratigraphic surfaces based on observations of stratal geometries and facies relationships, which we use for comparison to stratigraphic interpretations. We then apply both the trajectory analysis and the accommodation succession methods to manually map key stratigraphic surfaces and define sequence units on the final model output. Finally, we calculate shoreline and shelf-edge trajectories, the temporal evolution of changes in relative sea level (proxy for  $\delta A$ ) and sedimentation rate (proxy for  $\delta S$ ) at the shoreline, and automatically produce stratigraphic interpretations. Our results suggest that the analysis of the presented model is more robust with the accommodation succession method than with the trajectory analysis method. Stratigraphic analysis based on manually extracted shoreline and shelf-edge trajectory requires calibrations of time-dependent processes such as thermal subsidence or additional constraints from stratal terminations to obtain reliable interpretations. The 3-D stratigraphic analysis of the presented model reveals small lateral variations of sequence formations. Our work provides an efficient and flexible quantitative sequence stratigraphic framework to evaluate the main drivers (climate, sea level and tectonics) controlling sedimentary architectures and investigate their respective roles in sedimentary basin development.

## Publication Details

Ding, X., Salles, T., Flament, N. & Rey, P. (2019). Quantitative stratigraphic analysis in a source-to-sink numerical framework. *Geoscientific Model Development*, 12 (6), 2571-2585.



## Characterization of aerosols over the Great Barrier Reef: The influence of transported continental sources



Zhenyi Chen<sup>a</sup>, Robyn Schofield<sup>b</sup>, Peter Rayner<sup>b</sup>, Tianshu Zhang<sup>a</sup>, Cheng Liu<sup>a,c,d,\*</sup>, Claire Vincent<sup>b</sup>, Sonya Fiddes<sup>b</sup>, Robert George Ryan<sup>b</sup>, Joel Alroe<sup>e</sup>, Zoran D. Ristovski<sup>e</sup>, Ruhi S. Humphries<sup>f</sup>, Melita D. Keywood<sup>f</sup>, Jason Ward<sup>f</sup>, Clare Paton-Walsh<sup>g</sup>, Travis Naylor<sup>g</sup>, Xiaowen Shu<sup>a</sup>

<sup>a</sup> Key Lab of Environmental Optics and Technology, Anhui Institute of Optics and Fine Mechanics, Chinese Academy of Sciences, 230031 Hefei, China

<sup>b</sup> School of Earth Sciences, University of Melbourne, 3010 Melbourne, VIC, Australia

<sup>c</sup> School of Earth and Space Sciences, University of Science and Technology of China, 230026 Hefei, China

<sup>d</sup> Center for Excellence in Regional Atmospheric Environment, Institute of Urban Environment, Chinese Academy of Sciences, Xiamen 361021, China

<sup>e</sup> International Laboratory for Air Quality and Health, Queensland University of Technology, QLD 4000, Australia

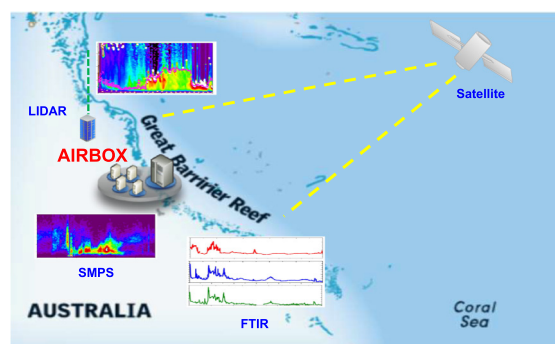
<sup>f</sup> Climate Science Centre, Oceans and Atmosphere, CSIRO, 3195 Aspendale, VIC, Australia

<sup>g</sup> School of Chemistry, University of Wollongong, 2522, NSW, Australia

### HIGHLIGHTS

- Simultaneous field observations of aerosols and marine boundary layer in Great Barrier Reef was investigated.
- A new layer of nucleation mode aerosols was observed with the averaged aerosol extinction coefficient of  $150 \text{ Mm}^{-1}$ .
- The marine boundary layer was characterized with two different regimes and compared with the results from WRF.
- The AOD and fire spots testified the pollution and backward trajectories indicated the transported continental sources.

### GRAPHICAL ABSTRACT



### ARTICLE INFO

#### Article history:

Received 8 March 2019

Received in revised form 29 May 2019

Accepted 1 July 2019

Available online 02 July 2019

Editor: Pingqing Fu

#### Keywords:

Aerosol  
LiDAR  
Boundary layer

### ABSTRACT

The rapid environmental changes in Australia prompt a more thorough investigation of the influence of transportation, local emissions, and optical–chemical properties on aerosol production across the region. A month-long intensive measurement campaign was conducted during spring 2016 at Mission Beach, a remote coastal site west of the Great Barrier Reef (GBR) on the north-east coast of Australia. One aerosol pollution episode was investigated in early October. This event was governed by meteorological conditions and characterized by the increase in black carbon (BC) mass concentration (averaged value of  $0.35 \pm 0.20 \mu\text{g m}^{-3}$ ). Under the influence of the continental transportation, a new layer of nucleation-mode aerosols with an initial size diameter of 20 nm was observed and aerosol number concentrations reached the peak of  $6733 \text{ cm}^{-3}$  at a diameter of 29 nm. The averaged aerosol extinction coefficient at the height of 2 km was  $150 \text{ Mm}^{-1}$ , with a small depolarized ratio (3.5–5%). Simultaneously, the boundary layer height presented a fall–rise trend in the presence of these enhanced aerosol concentrations and became stable in a later stage of the episode. We did not observe clear boundary layer height diurnal variations from the LiDAR observations or from the Weather Research and Forecasting (WRF) model outputs, except in an earlier stage of the aerosol episode for the former. Although the sea breeze

\* Corresponding author at: School of Earth and Space Sciences, University of Science and Technology of China, 230026, Hefei, China.  
E-mail address: [chliu81@ustc.edu.cn](mailto:chliu81@ustc.edu.cn) (C. Liu).

may have been responsible for these particles, on the balance of available data, we suggest that the aerosol properties at the GBR surface during this period are more likely influenced by regional transportation of continental sources, including biomass-burning aerosols.

© 2019 Elsevier B.V. All rights reserved.

## 1. Introduction

The wide-ranging effects of aerosols on the global radiative forcing system have received considerable attention over the last decade. They include the modification of radiation transfers and atmospheric photochemistry, cloud microphysical processes, and acidification of oceans by atmospheric sulfate or nitrate deposition (Ramanathan et al., 2001; Kaufman et al., 2002; Dusek et al., 2006; Doney et al., 2007). There have been a number of efforts to measure aerosols in urban, rural and remote sites around the globe. However, most of these studies were conducted in the Northern Hemisphere (Quinn et al., 2004; Lamarque et al., 2010; Bollasina et al., 2011; Wang et al., 2012). In the Southern Hemisphere, such as in Australia, significant gaps remain in the ability to accurately quantify aerosols at high temporal and spatial resolution. Satellite sensors such as Total Ozone Mapping Spectrometer (TOMS) used widely to map dust source area activity and Moderate Resolution Imaging Spectroradiometer (MODIS) to identify biomass-burning plume pathways face several key unresolved challenges. For example, Prospero et al. (2002) found the inability of TOMS to accurately identify shallow dust plumes. Myhre et al. (2008) argued that high aerosol optical depth (AOD) of biomass-burning emissions may be incorrectly screened out of the satellite data. Such limitations indicate that remote sensing of aerosols should be combined with surface-based observations to provide accurate information on aerosol characteristics. This approach has been used in large-scale field campaigns such as Mate 98 (Rosen et al., 2000), BIBLE-B (Takegawa et al., 2003), SAFIRE (Milic et al., 2017), and MUMBA (Guérette et al., 2017; Paton-Walsh et al., 2017). Although these measurements have provided much information on aerosols and trace gases in Australia, detailed vertical aerosol characteristics and transportation processes in this region are not fully understood.

Australia's Great Barrier Reef (GBR) is a unique location to study the aerosols and their potential influence on regional climate changes. In recent years, some studies have been conducted to characterize the sources, coastal nucleation, and evolution processes of aerosols over the GBR (Jones et al., 2007; Qin and Mitchell, 2009; Fischer and Jones, 2012; Leahy et al., 2013; Swan et al., 2016). Considering that Australia is mostly affected by smoke from controlled (planned) fires in the northern part of Australia (Tsumumi et al., 1999; Russell-Smith et al., 2007; Mitchell et al., 2013) and dust in central Australia (McGowan and Clark, 2008), the understanding of the impact of regional transportation on aerosol production and evolution properties in GBR is particularly important during the dry season when biomass burning is active in Northern and Eastern Australia (Carr and Keywood, 2005; Mallet et al., 2017).

Furthermore, an interpretation of aerosol measurements needs concomitant measurement of meteorological condition and boundary layer. Meteorological conditions including wind speed, wind direction, temperature and Relative Humidity (RH) play an important role in the physical and chemical modification of aerosols suspended in the BL. Meteorology also defines the atmospheric stability and therefore impacts on the atmospheric vertical mixing (O'Dowd et al., 2002; Charron et al., 2004). The spatial-temporal description of the marine boundary layer (MBL) is more complicated because it is close to the coast (Melas et al., 1995; Bates et al., 2002; Tomasi et al., 2011; Winning et al., 2017). Some scientific campaigns explored the impact of the evolution of the MBL in coastal sites, and its interaction with the sea breeze and solar radiation (Abbs and Physick, 1992; Donaldson and George,

2012; Ribeiro et al., 2018). However, there is still lack of the simultaneous observation of MBL vertical evolution and its relationship with meteorology such as wind in GBR.

This study investigated the time variation and climatology of aerosol loading and the MBL over the Great Barrier Reef. The paper is organized as follows: Section 2 describes the experimental setup and briefly summarizes the retrieval method for signal analysis. Section 3 includes the particle size distribution, vertical profiles of the aerosol extinction coefficients, depolarization ratios, and interprets the data. We compared MBL heights derived from LiDAR backscattered signals with results from the WRF model. Furthermore, back-trajectory analysis, MODIS AOD distribution, and World Fire Atlas hot spot detection were combined to track the origin of the air mass arriving at our observation site and the aerosol sources. Section 4 provides conclusions based on the measurement results in this experiment.

## 2. Materials and methods

### 2.1. AIRBOX and site details

In the austral spring of 2016 the Atmospheric Integrated Research Facility for Boundaries and Oxidative eXperiment (AIRBOX) was conducted to examine aerosol production and evolution from the Great Barrier Reef in more detail and to explore its influence on local and global climate. A range of measurements encompassing aerosols, trace gases, and meteorological parameters were made throughout the campaign. The AIRBOX facility was located at Mission Beach in Queensland, Australia, close to the south Coral Sea. Our observation site is a remote coastal headland located on the north-east coast of Australia (17.82250°S, 146.102365°E; Fig. 1), far from local anthropogenic sources of particles, such as roads. The intensive campaign was conducted for nearly a month, from 20 September to 16 October 2016.



Fig. 1. Map showing the Great Barrier Reef of eastern Australia. AIRBOX Ground Stations are located at Mission Beach.

## 2.2. Instrumentation

### 2.2.1. LiDAR

A Scanning Mini Micro Pulse LiDAR System (MiniMPL-532-C Micro, Sigma Space Corporation, Lanham, MD, USA) was installed and operated during the campaign period. The pulsed system operates at a wavelength of 532 nm, retrieves aerosol backscatter every 30 m, up to 9990 m, with a temporal resolution between 10 and 30 s. It has a cross-polarization detection channel, which enables the delivery of two-range and sky background-corrected parallel and perpendicular signals from the instrument's software. The overlapping factor between the laser beam and the field of view (FOV) became unity when the range from the LiDAR is 114 m. As a secondary product, the software computes the total backscatter coefficient. During operation, however, some gaps exist in the time series of the backscatter signals due to instrumental problems.

We calibrated the LiDAR by using clear-air signals in the far range for each profile. As multiple scattering effects can usually be neglected, accurate fields of the backscatter coefficient were derived, even though some uncertainties arise from the prescribed LiDAR ratio profile (Kovalev, 1995). We applied Fernald's (1984) algorithm to derive the extinction coefficient with the U.S. Standard Atmosphere (NOAA, NASA, USAF, 1976). The result of the analysis significantly depends on the LiDAR ratio  $S$  ( $S = \alpha/\beta$ ), where  $\alpha$  is the extinction coefficient and  $\beta$  is the backscattering coefficient. Therefore, we need an appropriate choice of  $S$ . To apply this method, we also needed a sufficient signal-to-noise ratio of the backscattering intensity at the far-side boundary range and a good estimation of the boundary value. We took the scattering ratio (SR) as 1.2 at the boundary height of 6 km; SR is defined as  $SR = (\beta_m + \beta_a)/\beta_m$ , where  $\beta_m$  and  $\beta_a$  are the backscattering coefficients of air molecules and aerosols, respectively.  $S$  was taken to be the constant value of 60, which is considered to be the representative value for mixed marine and urban aerosols at 532 nm (Franke et al., 2003; Ansmann and Müller, 2004). For signals with cloud deck, the reference height was chosen below the cloud height; thus, we retrieved aerosol extinction below and above the cloud deck by applying Fernald backward integration and forward inversion, respectively. Taking into account the unknown value of the LiDAR ratio and the assumed boundary condition, the errors calculated on the extinction profile were 15–20% in the center of the particle plumes discussed in this paper. Absolute errors were  $1.5 \times 10^{-4} \text{ Mm}^{-1}$ . We derived this number under the assumption of values of  $10\text{--}20 \text{ Mm}^{-1}$  ( $\text{Mm}^{-1} = 1 \times 10^6 \text{ m}^{-1} = 1 \times 10^3 \text{ km}^{-1}$ ) for the extinction coefficient. Depolarized ratio (DR) was defined as the ratio of components of backscattered light-powers polarized perpendicular and parallel to the plane of the polarization of the emitted laser. According to Mie-scattering theory, we expected the DR to be zero for single scattering by homogeneous and spherical particles (Cairo et al., 1999). The ratio of gains of the two Photomultiplier Tubes (PMTs) was determined within the 10% margin of error in the operating-voltage range.

### 2.2.2. SMPS

Particle number size distributions were measured by a Scanning Mobility Particle Sizer (SMPS) (TSI, Model 3080), with a custom-designed electrostatic classifier and a Condensation Particle Counter (CPC) (TSI, Model 3787). Prior to sampling, the aerosol was dried through a silica-gel diffusion dryer, followed by a membrane dryer (Nafion MD-700), bringing the sample to a mean RH of 30%. Then a well-defined charge distribution was applied to the sample by an X-ray aerosol neutralizer (TSI, Model 3087). Aerosols with diameters  $>615 \text{ nm}$  were removed with a  $0.0457 \text{ cm}$  impactor inlet and the aerosol size distributions were measured over the range of  $12\text{--}600 \text{ nm}$  with a time resolution of 3 min. Size distribution inversions were performed using the instruments built-in software export tool. Quality control/assurance procedures involved corrections for flow rate deviations, corrections for inlet losses as well as removal of faulty data.

### 2.2.3. FTIR and MAAP

Trace gas concentrations of CO and CO<sub>2</sub> were made with a spectronus greenhouse gas analyzer (Ecotech Pty Ltd., Australia). This analyzer uses a Bruker Fourier Transform InfraRed (FTIR) spectrometer (IRcube, Bruker Optics, Ettlingen Germany) and a temperature- and pressure-controlled White cell with 26 m path-length. Ambient air was sampled from the roof of AIRBOX and dried with Nafion and Magnesium perchlorate before passing to the White cell, where spectra were recorded every 5 min. Spectral analysis is via the spectrum model Multiple Atmospheric Layer Transmission (MALT) software (Griffith, 1996). The instrument was calibrated before and after the campaign and the instrument drift was monitored daily and corrected for using a stable cylinder of air. The analyzer makes continuous, simultaneous measurements of CO and CO<sub>2</sub>. A full description of the instrument is given by Griffith et al. (2012). Black carbon (BC) mass concentrations were obtained from a multi-angle absorption photometer (MAAP) (Thermo Scientific, Model 5012) using a 5-second sampling rate. The BC concentrations and standard deviations were calculated at a time resolution of 10 min. At this time resolution, the lower detection limit is estimated as  $<0.05 \mu\text{g m}^{-3}$ .

## 2.3. Synoptic setting

Fig. 2 shows the general synoptic situation during the Mission Beach campaign. This surface chart is from Australian Bureau of Meteorology (BOM). The experimental location is marked by a blue circle on the image. On 4 October, a high-pressure system caused advection of background air from continental Australia. The ridge of high pressure lay ahead of a vigorous cold front associated with a depression in the Southern Ocean. The high pressure reached the Coral Sea on 6 October with a core pressure of 1023 hPa and the continental air was advected from western Australia. The core region of this elongated high-pressure system was usually clear. The general weather situation did not change substantially, and the anticyclonic flow persisted in eastern Australia. Correspondingly, airflow was nearly stagnant, and the days during this period were characterized by weak winds from the east and southeast. After the high pressure had moved on, Mission Beach began to be affected by anticyclonic subsidence. Our observing site was influenced by disturbances passing from western to eastern Australia during this observation period, and these disturbances also pushed low-level clouds from inland.

## 3. Results and discussion

Our campaign observed a mixture of terrestrial, biomass-burning, and marine conditions during the one-month observing period. In the earlier period, the aerosols in GBR were more dominated by the marine aerosols (sea-salt). However, the marine condition was then followed by a transition to continental-influenced condition. Two biomass-burning emission events were observed from 3 October to 9 October and from 12 October to 16 October 2016, respectively. In particular, we found the high concentration of small particles (with diameters of  $<30 \text{ nm}$ ) transported to the GBR region during the first biomass-burning episode. Therefore we selected the dates from 3 to 9 October to investigate the aerosol properties in GBR because: (1) they corresponded to periods where surface southeasterly winds were dominant, (2) enhanced aerosol extinction as well as decreased depolarized ratio could be measured, and (3) particle size distribution experienced a sudden shift to smaller sizes. Specifically, this section describes the general features of the observations and discusses the results of LiDAR, SMPS, and the boundary layer evolution with reference to the surface meteorological data. In the data analysis, the time coordinate used was local standard time (LST), which equates to coordinated universal time (UTC) + 10 h.

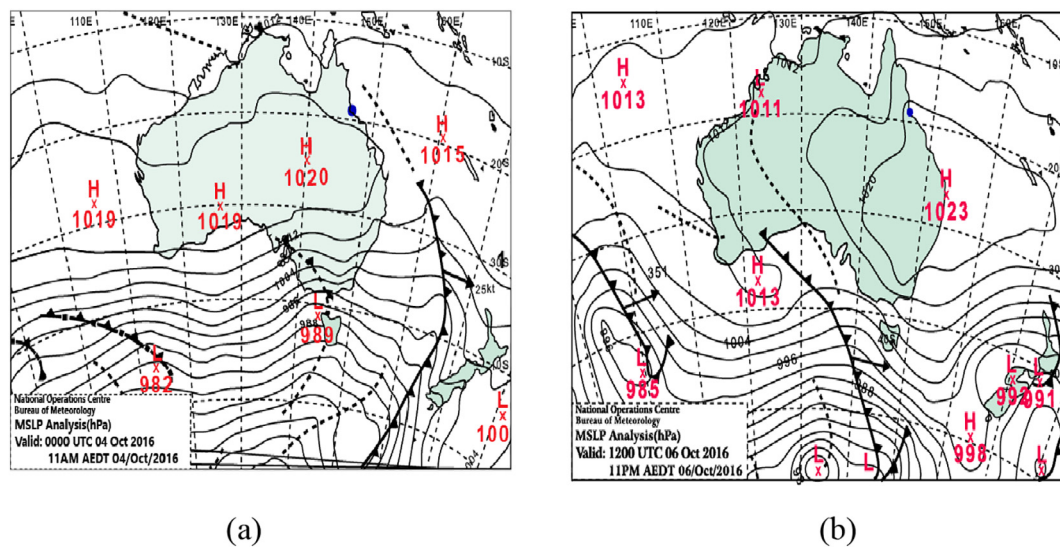


Fig. 2. Surface chart at 12:00 UTC on 4 October and 6 October 2016. (Source: Australian Bureau of Meteorology (BOM).)

### 3.1. Overview

We measured the temperature, atmospheric pressure, solar irradiance, wind speed, wind direction, and RH in 5-min intervals (Fig. 3). The wind direction fluctuated on 8 October and varied gradually from northerly to southerly wind from that afternoon onward. Then, the southeasterly wind ( $\sim 120^\circ$ ) remained rather constant from noon of 4 October until 9 October. Wind speed was below 4 m/s throughout the event, with gradual decreased wind speeds down to 0.5 m/s on 9 October (Fig. 3a), which were consistent with the passing high-pressure system. Because the wind speed was in the low-pressure region of  $< 4$  m/s, it was chosen to represent aerosols not generated by wind-driven processes over the ocean (Prijith et al., 2014; Ribeiro et al., 2018). RH and air temperature showed a more negative relationship throughout the entire observation period (Fig. 3b). Specifically, RH ranged from around 96% to 50% with a decreasing trend from 4 to 7 October. The air temperature was more stable and varied between  $22^\circ\text{C}$  and  $30^\circ\text{C}$ . The wind direction from the east was consistent and RH decreased simultaneously with the drop in particle size distribution from 4 October (see Section 3.2.1), suggesting a change air flow of the observation. Fig. 3 (c) shows the time-series of CO, CO<sub>2</sub>, and BC. The episode is also evident in the trace gas time-series, with the peak concentration of CO above 140 ppb during the late hours of the 3 October (20:54 pm) and CO<sub>2</sub> above 460 ppm in the early morning of 4 October (00:52 am), respectively. CO remained above 90 ppb until 3 pm on 4 October. Strong simultaneous enhancements are also found at this time in BC concentration, reaching above  $1.091 \pm 0.076 \mu\text{g m}^{-3}$  within a few hours on 3 October. The mass concentrations maintained high levels with the averaged value of  $0.35 \pm 0.20 \mu\text{g m}^{-3}$  on 4 October and then decreased in the following days. In fact there was clear indication of an enhancement in CO in the form of two large peaks late on 3 October and again in the early part of 6 October, while the second peak of CO<sub>2</sub> and BC concentration occurred later on 6 October afternoon. These coincident peaks indicate similar pollution sources.

Fig. 3(d) illustrates the time sequence plots of the range-corrected signals measured by LiDAR during the observation period. The color bar indicates the signal's intensity in counts km<sup>2</sup>/us. The detailed vertical structures of the aerosols reached an altitude of 5.0 km above ground level (AGL) and confirmed the presence of aerosol-layering activity. LiDAR also captured the MBL height evolution from a fluctuated into a well-mixed structure. Furthermore, some precipitation, fog, and cloud events in this area contaminated the aerosol profiles by adding multiple crests and troughs to the signal. The effect of these events normally

is attenuated by time and vertical averaging of the instantaneous profiles.

### 3.2. Aerosol physical-optical properties

#### 3.2.1. Size distribution

Particle number size distributions are among the most important parameters in trying to understand the characteristics of particle population. Fig. 4 illustrates total number size distribution from 3 to 9 October (LST). As shown, the particle number size distributions were dominated by well-defined Aitken ( $20 \text{ nm} < D_p < 100 \text{ nm}$ ) and accumulation modes ( $100 \text{ nm} < D_p < 800 \text{ nm}$ ). The mean and median of number concentration for the size range 12–150 nm over the period of 4–6 October was  $2.9 \times 10^3 \text{ cm}^{-3}$  and  $1.5 \times 10^3 \text{ cm}^{-3}$ , respectively. The mean modal diameters of the Aitken ( $\approx 55 \text{ nm}$  at 30% RH) and accumulation ( $\approx 150 \text{ nm}$  at 30% RH) modes were both higher (a factor of 1.3 for Aitken modes and a factor of 1.15 for accumulation modes) than that measured in the subtropical Northern and Southern Hemisphere regions (Bates et al., 2002). The two peaks of aerosol number concentrations were found on 4 October in the Aitken mode (6733 particles  $\text{cm}^{-3}$  at diameter of 29 nm) and 6 October in the Aitken mode (5343 particles  $\text{cm}^{-3}$  at diameter of 59 nm), respectively.

Usually, the fluctuation in the particle number concentration is most likely caused by coagulation, primary particle emissions, and wind speed and planetary boundary layer (PBL) variations. In the initial stage of the event, a third mode (nucleation mode,  $5 \text{ nm} < D_p < 20 \text{ nm}$ ) was observed in the afternoon of 3 October, coinciding with the dramatic wind direction change and rather fluctuant wind speed. Although the number size distribution shows a clear nucleation mode, this feature was only present for less than half a day. This is because the one-day cold fronts (Fig. 2) passing through the observing area mixed nucleation-mode particles into the MBL, the short MBL residence time provided little time for particle growth. Another possible reason is that the nucleation-mode aerosol may have been emitted from a short-term source nearby our sampling site (e.g. a localized biomass-burning event). This would mean that the aerosol would not have had much opportunity for growth before being sampled.

Notably, the event took place when RH was increasing and temperature was decreasing, showing the opposite pattern of typical new particle formation events. Therefore the elevated number concentrations were more likely from transported continental aerosols such as a biomass-burning particles. After the decrease of nucleation-mode particles, the number concentration features a dominant mode in the

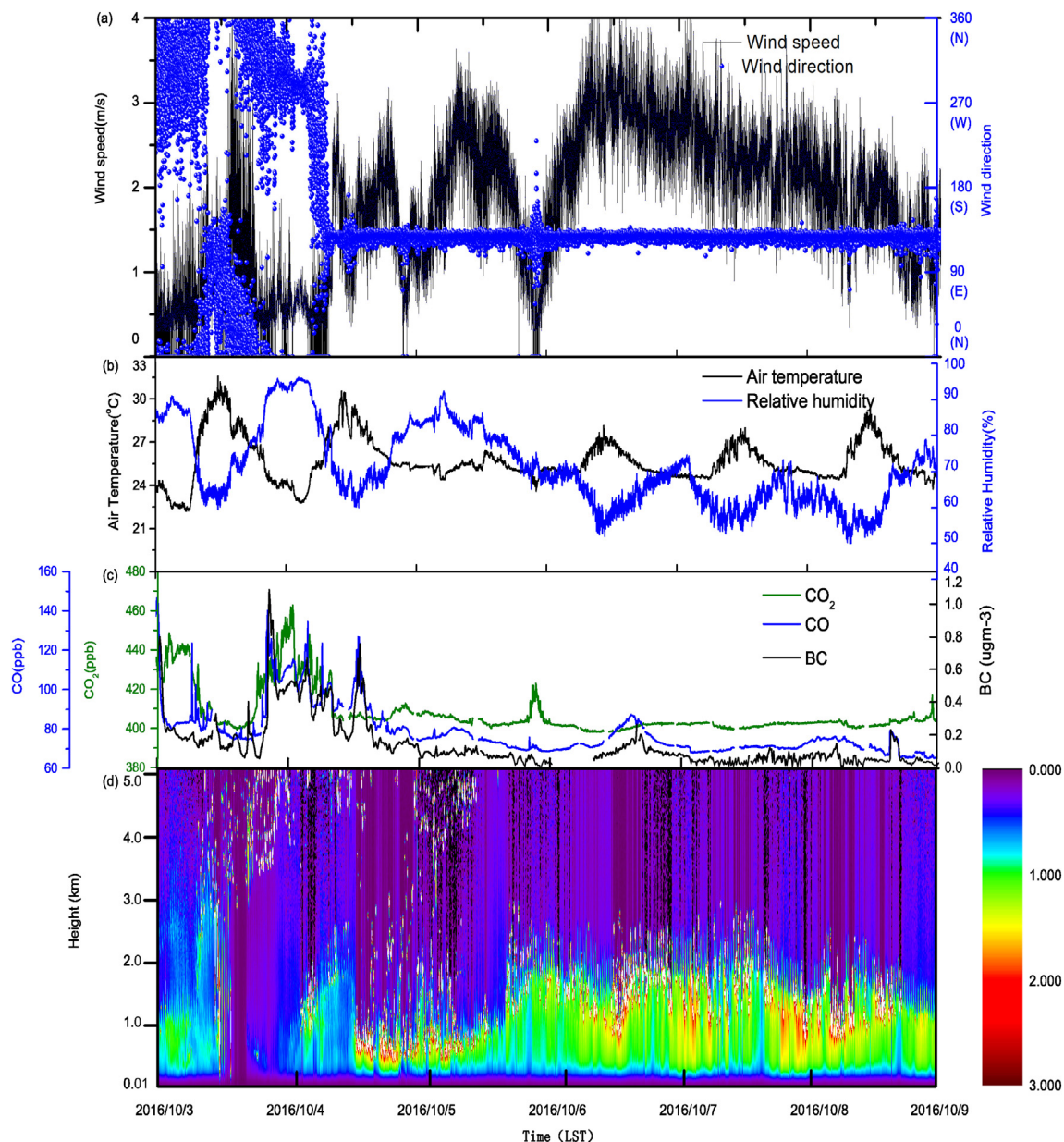


**Fig. 3.** Meteorological parameters, lidar backscattered signals and in-situ trace gas and BC measurements from 3 October to 9 October. (a) In situ wind direction during the period was constantly from the east, with minimal variation. Wind speed was low throughout the event, remaining below 4 m/s. (b) The event saw an overall trend of slight decrease in RH that was simultaneous with stable air temperature. (c) CO, CO<sub>2</sub> and BC mass concentration showed simultaneous peaks on in the late hours of 3 October and maintained high levels to 4 October. The second peak of CO, CO<sub>2</sub> and BC mass concentration was observed on 6 October. (d) Cross-section of aerosol optical backscattering at 532 nm from the ground to 5.0 km AGL over a 2-min-averaged period collected in Mission Beach, Australia was found to reach higher levels from 4 October.

particle size distribution centered around  $D_p \approx 70$  nm until 6 October. Beginning 7 October, the particle diameter increased to the range of 100–200 nm, which may have been the result of aging processes of biomass-burning aerosols, mixed with additional marine aerosols. This tendency is consistent with Australia's biomass-burning aerosol averaged size of 110 nm (Radhi et al., 2012; Milic et al., 2017).

### 3.2.2. Extinction coefficient

The profiles of the extinction coefficients were smoothed with 60 m. As can be seen in Fig. 5, the profiles of the optical properties were split into sublayers of variable heights. The polluted MBL reached 1.0 km. The extinction coefficients at 0.6 km on 4 October and 6 October showed significant enhancements and the extinction values were high ( $50\text{--}150 \text{ Mm}^{-1}$ ) in the lofted tropospheric aerosol layer. Aerosols above 1.0 km were fairly constant, indicating that the well-defined MBL provided a strong barrier to the vertical transport of biomass-

burning emissions over land. The 532-nm AOD was close to  $0.13$  in the episode. The aerosol extinction coefficient decreased to  $60 \text{ Mm}^{-1}$  on 8 October and the polluted layer rose to a height of 0.8 km. The averaged AOD on 8 October was 0.03, and the values in the remaining days rarely exceeded a background level of 0.1, which was consistent with the average AOD value in Australia (Radhi et al., 2009).

### 3.2.3. Depolarization ratio

On a vertical scale, we generally observed a Depolarization Ratio (DR) larger than 0.02 in the MBL. We omitted the DR profiles above 2 km because of the low signal-to-noise ratio and the low percentage of DR ( $\sim 2\%$ ) even under moderate aerosol-loading conditions in spring. The temporal variations of DR on 4, 6, and 8 October are shown in Fig. 6. The profile of DR ranged from about 7% to 8% on 4 October in the lower troposphere and decreased with increasing heights. The DR value decreased and reached the minimum value of 3% on 6 October, indicating

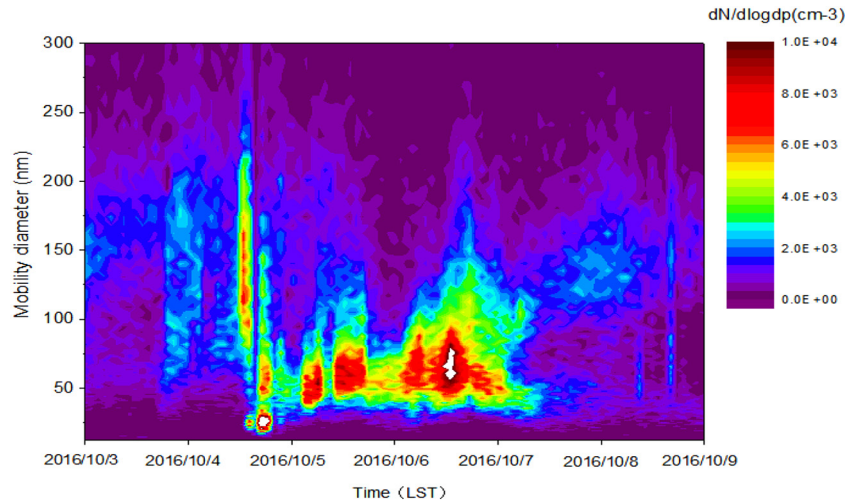


Fig. 4. Contour plots of aerosol size distribution from 3 October to 8 October 2016. Aerosol concentrations per diameter bin are given in terms of  $dN/dlogdp$ .

the influence of different aerosol sources, whereas the concentration of aerosols was relatively high in the MBL (shown in Figs. 4 and 5). On 8 October, the DR increased again to a higher value of 12%. Although we conducted our measurement along the coast of Mission Beach, sea-breeze wind strengths were low, meaning that the measurement was less related to the effect of the internal boundary layer (Garratt, 1992). The boundary structure will be investigated in Section 3.3.

To investigate the aerosol source, we took the averaged values of DR between 110 m and 149 m in altitude as representative values of DR in the lower atmosphere and RH at ground level (see Fig. 7). Temporal changes of DR and RH were presented under fair weather (i.e., fine and weak-wind conditions between 4 and 8 October) (see Fig. 6). The DR values dropped from 8% to 3.7% in the morning of 4 October, and then DR converged to small values and fluctuated between 3.5% and 5.5% until 6 October. We also observed a positive correlation of averaged DR and RH on 4 October with the correlation coefficient of 0.64. The contribution of aerosols to the observed or total DR depends mainly on the aerosol DR and the concentration of aerosols. If the aerosols in the MBL are hygroscopic or water soluble, they should absorb more water from

the surrounding humid air, swell, and become more spherical as a result of the surface tension of the liquid phase. Moreover, their scattering efficiency should increase according to the increase in size, and consequently, DR should decrease. However, the reverse took place in our observation: DR decreased and the aerosol size shifted to a smaller scale (Fig. 4) as RH decreased. This finding supports our assumption that the aerosols are more likely continental aerosols with low hygroscopicity in this case. Then, the negative correlation between DR and RH was observed from the early hours of 8 October, with the correlation coefficient of 0.64. It suggests more hygroscopic or water-soluble particles such as sulfates and nitrates, and deliquescent particles such as NaCl.

### 3.3. Boundary layer height

The boundary layer height determines the depth of the troposphere directly influenced by the Earth's surface (Stull, 1988). Aerosol vertical distribution is strongly influenced by boundary layer thermal structures, which are different over land and the ocean. Generally, LiDAR

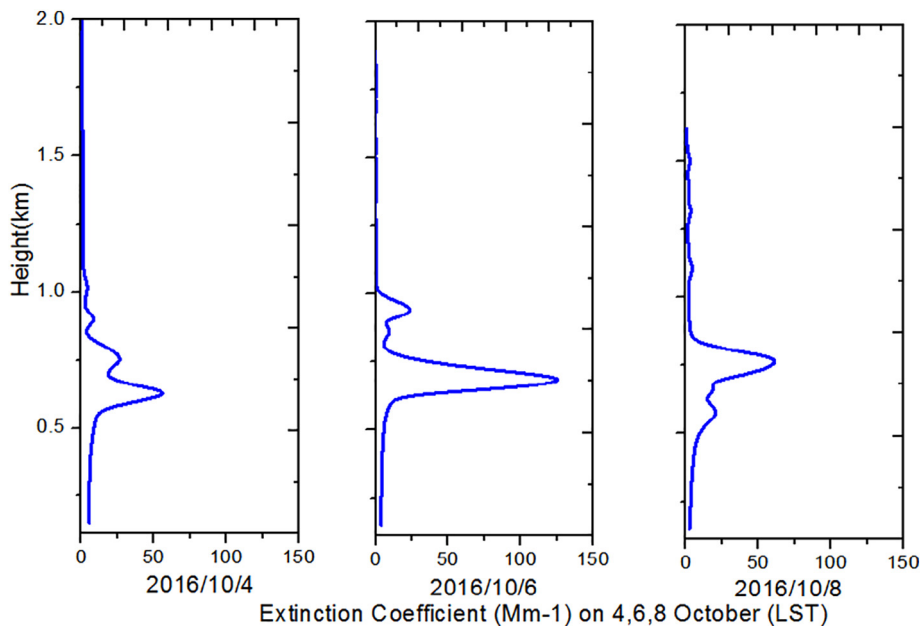


Fig. 5. Profiles of (a) extinction coefficient and (b) DR measured on 4 October 2016. Error bars denote standard deviations caused by signal noise and systematic errors from the estimates of input parameters. Only profiles higher than 0.1 km are trustworthy because of an overlap effect.



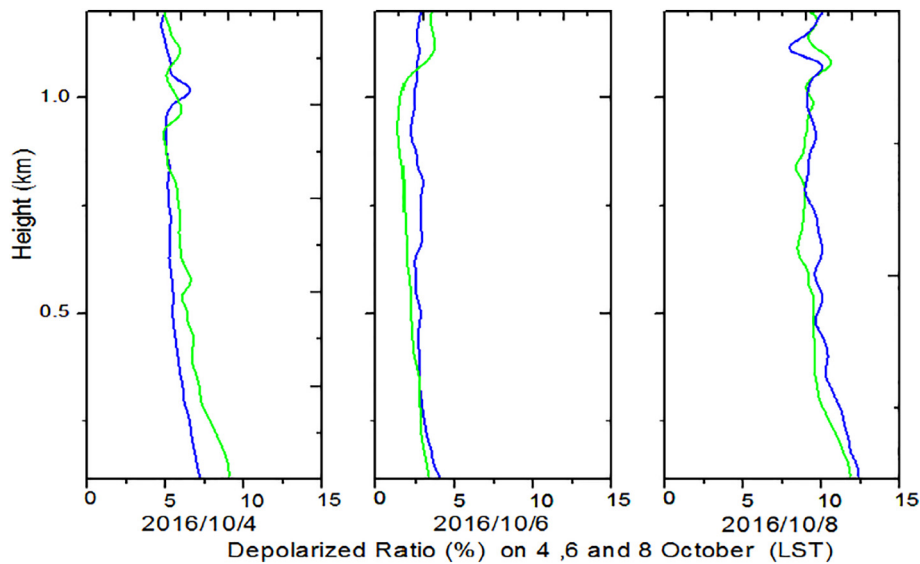


Fig. 6. Vertical profiles of the DR on 4, 6 and 8 October 2016.

signal intensity decreases from the top of the boundary layer to the free troposphere in the absence of a cloud layer or residential layer (Luo et al., 2014). Among different LiDAR-based boundary layer detecting methods, the gradient of the range-corrected signal and the Haar wavelet transform (Brooks, 2003; Baars et al., 2008) to measure the fluctuations of the signal represent the most commonly used techniques (Flamant et al., 1997; Lammert and Bösenberg, 2006). Both these methods rely on the fact that most of the pollutants, like aerosols, are concentrated in the boundary layer. Here we used the Haar wavelet transformation of the LiDAR-backscattered signal to estimate the boundary layer height and compared our estimates with the WRF simulations. The WRF model (Borge et al., 2008; Pichelli et al., 2014) was used to differentiate the boundary layer top by identifying an inversion in the temperature and humidity data.

Fig. 8 shows the two different regimes of boundary layer evolution derived from LiDAR backscattered signal on 4 and 6 October. Temporal and spatial resolutions were 2 min and 30 m, respectively. One regime occurred during the drastic variation of boundary layer and another with a regime of equilibrium entrainment (i.e., when boundary layer evolution was in a quasi-steady state). 4 October coincided with the first part of the period of consistent southeasterly winds. The boundary layer height decreased gradually in the early morning, reaching the minimum height of 0.2 km and remained still until 10:00 LST. Then

boundary layer height increased gradually to 2.0 km before it experienced a sharp decrease again to 0.3 km at 18:00 LST. In comparison the aerosol layer on 6 October became rather stable and was trapped in the entrainment region. We did not find a clear diurnal variation for boundary layer height observations from the LiDAR aerosol-related signals except those taken on 4 October.

The boundary layer height estimates from WRF generally were lower than those from the LiDAR observations, especially on 4 October when the boundary layer fluctuated strongly. In the WRF formulation, the boundary layer height was a function of the bulk Richardson number, which depended on the temperature and wind speed profile. Compared with the surface variables, vertical profiles from the lidar were less dependent on the surface-layer schemes. The surface-layer parametrizations contributed only to near-surface variability in both the unstable and stable regimes, whereas the shapes of the profiles were determined by the boundary layer mixing algorithms. Our results agree with those by Krogsæter et al. (2011), who also found WRF underestimated boundary layer height when compared with observations at the offshore research platform in the North Sea and rather low boundary layer height during springtime.

### 3.4. Possible particle sources

#### 3.4.1. MODIS AOD and fire spots

Fig. 9 shows the integration of the MODIS-retrieved AOD at 550 nm on 4 October and the fire spots based on level 2 Terra/MODIS thermal anomalies/fire product (MOD14) from 27 September to 7 October. In this study, we used MODIS Level\_2 AOD product (MOD/MYD04) over ocean and land at 0.55  $\mu\text{m}$ , which are available at 3 km  $\times$  3 km spatial resolution. The retrieval algorithm is based on the look-up table (LUT) approach, which employs a predefined set of aerosol types, loadings, and geometries. To account for both land and ocean, we used dark target algorithm retrievals instead of deep blue algorithm retrievals, which can be used only over land. This approach detected AOD and fire spots simultaneously. The small-depolarized ratio in Fig. 6 indicates that fine-mode particles were the major contributor to the days of aerosol optical thickness during this episode. During the late dry season (from September to November), biomass-burning aerosol contributed significantly to the aerosol optical thickness, in particular on moderate AOD days, which is as expected given that biomass burning was active in eastern and northern Australia during much of this observation period.

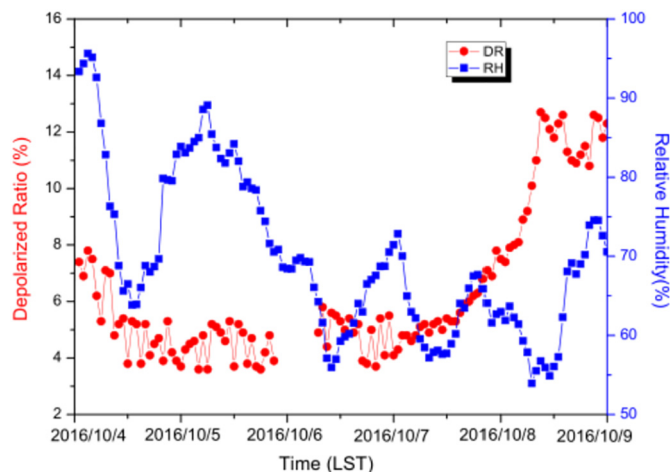
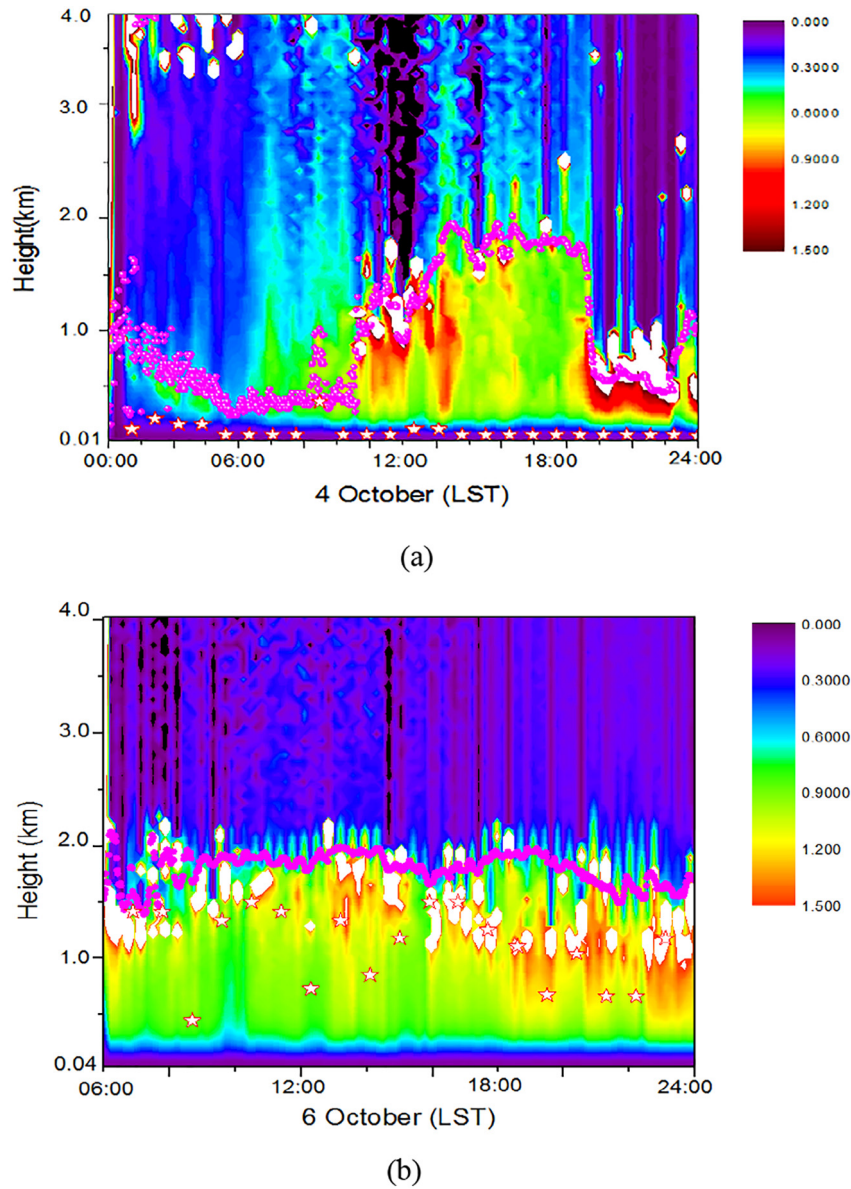


Fig. 7. Temporal changes of averaged DR and surface RH in the lower atmosphere.



**Fig. 8.** Time-height cross-section of the range-square-corrected backscatter signal, measured on (a) 4 October and (b) 6 October 2016 (6 October starts from 06:00 LST because of instrument breakdown). The color bar indicates the lidar backscattered-signal's intensity. Magenta circles and red stars indicate the BLH estimates from the maximum gradient of the wavelet analysis and the estimate from WRF, respectively. (For interpretation of the references to color in this figure legend, the reader is referred to the web version of this article.)

#### 3.4.2. Back-trajectory air mass

To understand the changes in aerosol data, the various influences on the air mass must be characterized to determine the possible sources and sinks. We achieved this by considering synoptic conditions, measuring in situ meteorology, and calculation of back-trajectories using the Global Data Assimilation System (GDAS) global data set in the Hybrid Single Particle Lagrangian integrated trajectory (HYSPLIT) model (Draxler, 2003; Rolph et al., 2014). For an unusual air mass (e.g., BLH rapid-change episode), we calculated 72-h back-trajectories at altitudes of 1.0 km to observe the passage of air in the MBL before the air arrived at Mission Beach.

The calculated HYSPLIT back-trajectories indicated that almost all of the air masses experienced an anticlockwise path on 3, 4, 6 and 8 October (Fig. 10). On 3 October, air masses that had originated over the ocean region spent at least 72 h traveling over the Coral Sea within the MBL and crossed land briefly before arriving at the observation sites. This movement implied that the MBL on that day should contain more maritime aerosols, with small contribution from continental aerosols. Then on 4 and 6 October, the air masses passed through burning

areas of northern and central Australia, recirculating the mixed aerosol air masses, which would bring additional biomass-burning aerosol. A small contribution from the Lake Eyre Basin secondary aerosol components, such as nitrates and organic acid ions, were also possible. Therefore these trajectories gave a meso-scale spatial bound to the conditions leading to the layer of smaller-size particles shown in Fig. 4, rather than the local scale. On 8 October, the air masses traveled across the Coral Sea again after a long-distance transportation from southern and central Australia. The fine-mode peak shifted to a larger radius with lower concentrations in the accumulation mode, which may have been due to a reduction in the number of particles as a result of aging processes and more marine aerosols.

#### 3.4.3. Sources

Aerosols in the MBL are locally emitted, wind-driven particulates and have the greatest variability in composition and concentration. Here, we give one possible interpretation of the observed results by considering the optical properties of aerosols. Before the noon of 3 October, more marine aerosols, including sea-spray aerosol, contributed to the

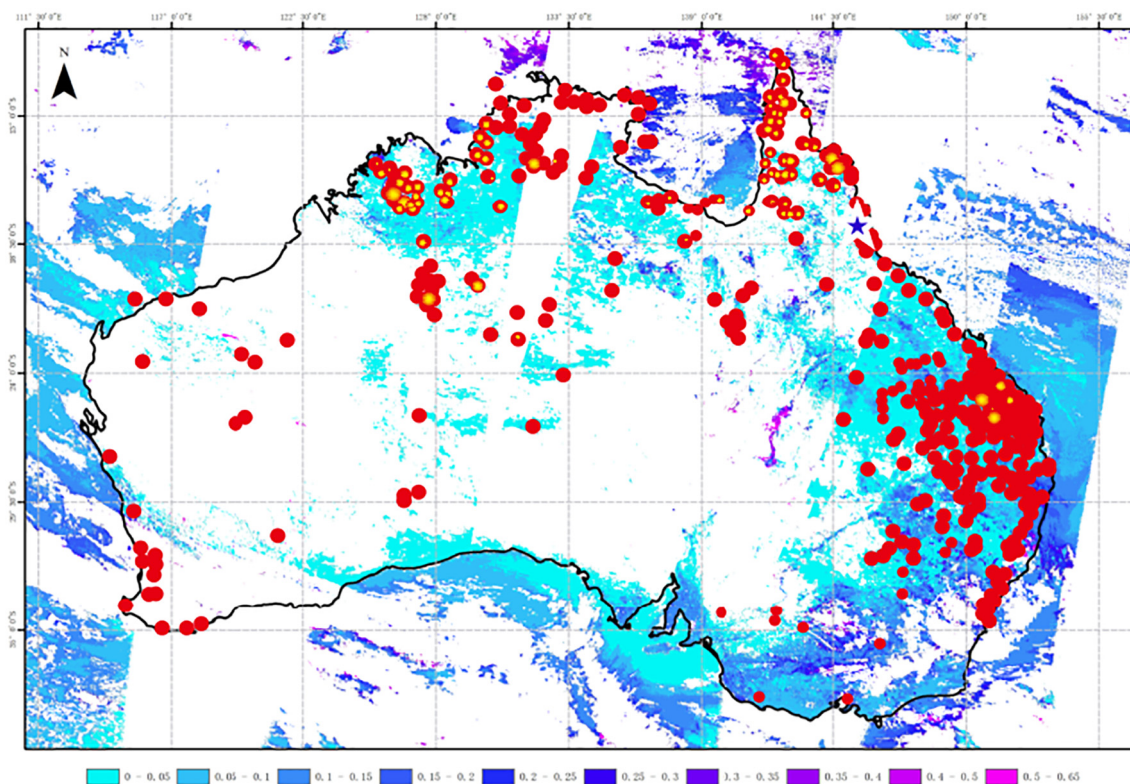


**Fig. 9.** MODIS-derived AOD observed on 4 October 2016 and MODIS fire map during the observing period.  
Source: <http://ladsweb.nascom.nasa.gov> and <http://lance.modaps.eosdis.nasa.gov/cgi-bin/imagery/firemaps.cgi>.

overall mass of MBL aerosols. From the afternoon of 3 October, the aerosol size decreased rapidly from 100 nm to 20 nm with a dramatic wind shift, and then the size distributions were dominated by well-defined Aitken mode until 7 October. The change in wind direction from the marine and coastal sectors to the continental sector was accompanied by an appearance of relatively smaller-sized particles. This indicated that the cleaner, marine air containing the dominant seasalt and sulfate aerosols were replaced by continental air masses as the local wind changed direction from sea to land.

There is further evidence suggesting that the layers of aerosols were of continental origin. Although back-trajectories might be fairly uncertain, we propose with some confidence that the air masses passing over northern and central Australia spent very little time over the local GBR. Therefore, it would appear to be fairly improbable that the majority of the layer contents are of recent GBR origin, and subsequently, they most likely reflect a transport phenomenon involving distant sources. We know that biomass burning constitutes a large source of dry-season aerosol emissions over northern and central Australia, and episodic austral summer wild fires in southern and eastern Australia. Because our observation campaign began in the late dry season in October and November, we can assume that some of the aerosols were from continental sources, especially biomass burning, and that they contained more organic components. Measurements of anthropogenic or continental tracers (e.g., CO) could also prove this hypothesis though we could not totally rule out marine and coastal sources. Therefore, we suggest that the GBR was more likely influenced by the transportation sources mixed with small amounts of marine aerosols in this event. The long-distance transportation of continental aerosols contributed a major source of fine particles in the GBR and played a significant role in local climate.

#### 4. Conclusions

We analyzed the aerosol observations at a coastal site near the GBR using LiDAR measurements, SMPS, and meteorological parameters

(such as measured wind direction and speed and back-trajectories) to understand the processes. We observed an enhancement of the aerosol layer at a height of 0.6 km on 4 October and 6 when the north-westerly air mass persisted and combined with stable meteorology. The averaged aerosol extinction at a height of 0.6 km was  $150 \text{ Mm}^{-1}$  for the MBL. Integrating the extinction coefficient from 0.1 km to 0.8 km, we identified a corresponding aerosol optical depth of 0.13. We generally observed a positive correlation between DR and RH in the lower atmosphere. A possible explanation for this observation was biomass-burning aerosols that produced new particles as a result of the long transportation of biomass-burning aerosols from eastern and central Australia.

Although single-wavelength elastic LiDAR measurements are necessarily limited in space and time and in their ability to differentiate among various types of aerosol particles, LiDAR measurements with aerosol optical properties can be taken in two or three dimensions and in time by performing process research (field studies). These measurements are beneficial to improving our understanding of aerosol sources and processes. Further systematic studies should be combined with additional surface-based observations to provide more accurate information on aerosol characteristics. It also appears that the GBR is a particularly dependable and productive location for studies dealing with the evolution and fate of long-distance-transported biomass-burning products. This understanding of possible transported sources needs to be improved, especially over tropical regions where inputs of biomass burning to the ocean are predicted to increase over the next century (Keywood et al., 2013). Accordingly, the need for observational data from biomass-burning source areas is undeniable, particularly that which quantifies the physical attributes of smoke plumes, their relationship to source area surface characteristics, land use, and synoptic and local-scale meteorology.

#### Data availability

Lidar and meteorologic data are available upon request to Robyn Schofield ([robyn.schofield@unimelb.edu.au](mailto:robyn.schofield@unimelb.edu.au)) at University of

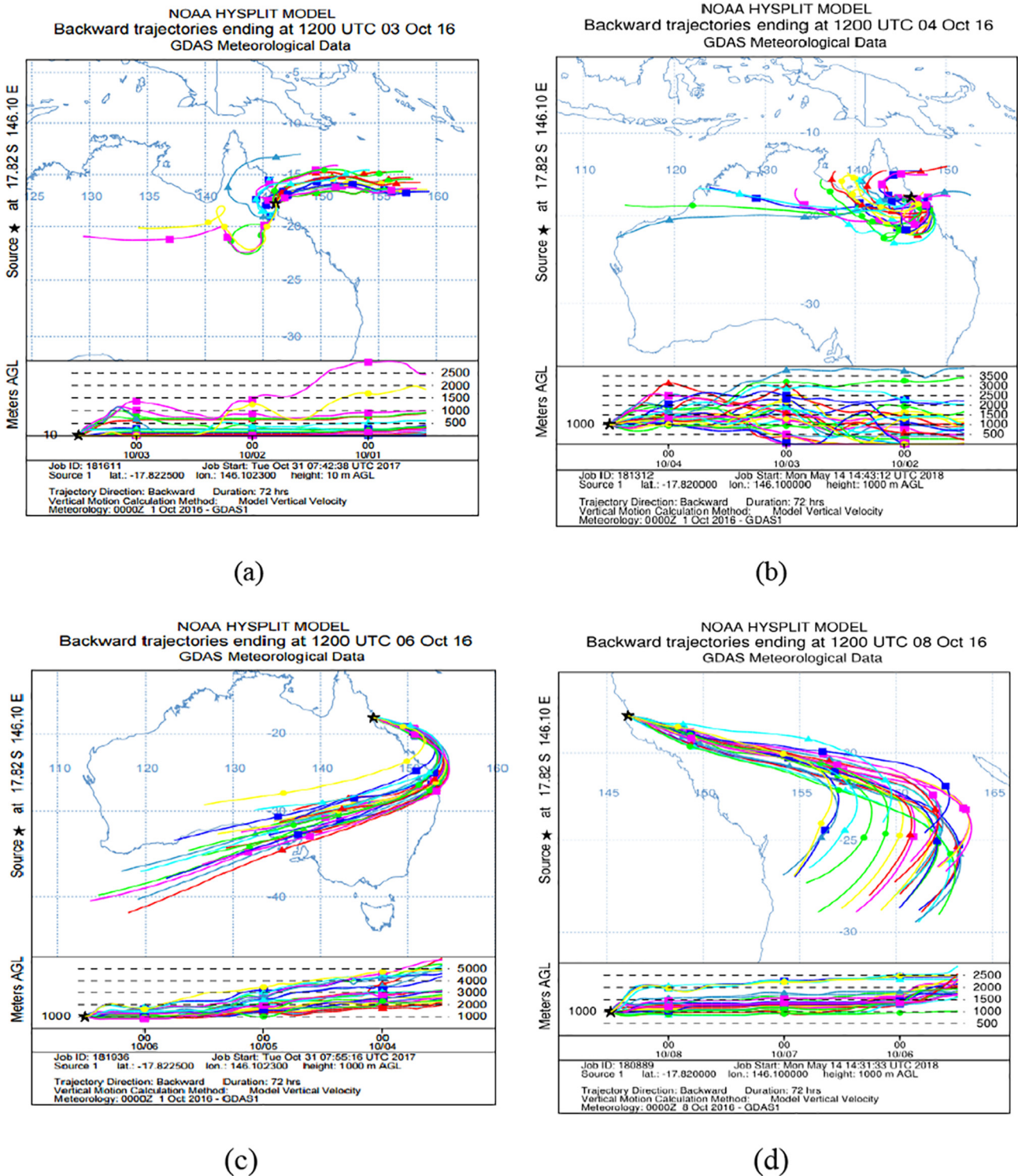


**Fig. 10.** (a)–(d) Backward trajectory ensembles at 0.1 km ending at Mission Beach, Eastern Australia, at 12:00 UTC on 3, 4, 6, October and 8 October 2016. The plot is presented according to the HYSPLIT calculation scheme.

Melbourne. SMPS and BC data are available upon request to Zoran Ristovski ([z.ristovski@qut.edu.au](mailto:z.ristovski@qut.edu.au)) in Queensland University of Technology. Trace gas data are available upon request to Clare Paton-Walsh ([clarem@uow.edu.au](mailto:clarem@uow.edu.au)) at University of Wollongong.

**Author contributions**

Zhenyi Chen wrote the manuscript and made the overall data analysis. Robyn Schofield, Robert George Ryan and Sonya Fiddes provided

meteorological data and ran the lidar measurements. Claire Vincent calculated tabulated WRF data. Joel Alroe and Zoran D. Ristovski carried out the SMPS measurements and performed quality control. Ruhi S. Humphries, Melita D. Keywood and Jason Ward provided MAAP instrumentation. Joel Alroe and Zoran D. Ristovski also operated MAAP and collated the black carbon data. Clare Paton-Walsh and Travis Naylor provided in situ gas-phase results. Robyn Schofield, Peter Rayner, Tianshu Zhang, Cheng Liu, and Xiaowen Shu provided academic support.

## Acknowledgement

The AIRBOX container and many of the instruments used in this campaign were funded by the Australia Government via the Australia Research Council LIEF funding (LE150100048). The field work was supported by the ARC Discovery project (DP150101649). Robyn Schofield was supported by Australian Research Council's Centre of Excellence programs (CE110001028 and CE170100023). Zhenyi Chen was supported by Youth Innovation Promotion Association CAS, and National Key Research and Development Program of China (2018YFC0213100, 2017YFC0213002). The authors also gratefully acknowledge the NOAA Air Resources Laboratory (ARL) for providing the HYSPLIT transport and dispersion model used in this research. The synoptic information are from the Australian Bureau of Meteorology.

## References

- Abbs, D.J., Physick, W.L., 1992. Sea-breeze observations and modelling: a review. *Aust. Meteorol. Mag.* 41, 7–19.
- Ansmann, A., Müller, D., 2004. Lidar Range-Resolved Optical Remote Sensing of the Atmosphere. chap. 4. Springer, New York, p. P112.
- Baars, H., Ansmann, A., Engelmann, R., Althausen, D., 2008. Continuous monitoring of the boundary-layer top with lidar. *Atmos. Chem. Phys.* 8, 7281–7296.
- Bates, T.S., Coffman, D.J., Covert, D.S., Quinn, P.K., 2002. Regional marine boundary layer aerosol size distributions in the Indian, Atlantic, and Pacific oceans: a comparison of INDOEX measurements with ACE-1, ACE-2, and Aerosols 99. *J. Geophys. Res.* 107 (D19), 8026. <https://doi.org/10.1029/2001JD001174>.
- Bollasina, M.A., Ming, Y., Ramaswamy, V., 2011. Anthropogenic aerosols and the weakening of the south Asian summer monsoon. *Science* 334 (6055), 502–505. <https://doi.org/10.1126/science.1204994>.
- Borge, R., Alexandrov, V., José, del V.J., Lumbrales, J., Rodríguez, E., 2008. A comprehensive sensitivity analysis of the WRF model for air quality applications over the Iberian Peninsula. *Atmos. Environ.* 42 (37), 8560–8574.
- Brooks, I.M., 2003. Finding boundary layer top: application of a wavelet covariance transform to lidar backscatter profiles. *J. Atmos. Ocean. Technol.* 20, 1092–1105.
- Cairo, F., Donfrancesco, G.D., Adriani, A., Pulvirenti, L., Fierli, F., 1999. Comparison of various linear depolarization parameters measured by lidar. *Appl. Opt.* 38, 4425–4432.
- Carr, S. B., Gras, J., Hackett, M., and Keywood, M.: Aerosol Characteristics in the Northern Territory of Australia During the Dry Season with an Emphasis on Biomass Burning, DTIC Document, 2005.
- Charron, A., Birmili, W., Harrison, R.M., 2004. Sources and Processes that Influence Particle Size, Number and Mass at a Rural Site in England (Harwell). Report to DEFRA, London.
- Donaldson, D.J., George, C., 2012. Sea-surface chemistry and its impact on the marine boundary layer. *Environ. Sci. Technol.* 46, 10385–10389.
- Doney, S.C., Mahowald, N., Lima, I., Feely, R.A., Mackenzie, F.T., Lamarque, J.-F., Rasch, P.J., 2007. Impact of anthropogenic atmospheric nitrogen and sulfur deposition on ocean acidification and the inorganic carbon system. *Proc. Natl. Acad. Sci. U. S. A.* 104 (37), 14580–14585.
- Draxler, R.R., 2003. Evaluation of an ensemble dispersion calculation. *J. Appl. Meteorol.* 42, 308–317.
- Dusek, U., Frank, G.P., Hildebrandt, L., Curtius, J., Schneider, J., Walter, S., Chand, D., Drewnick, F., Hings, S., Jung, D., Borrmann, S., Andreae, M.O., 2006. Size matters more than chemistry for cloud-nucleating ability of aerosol particles. *Science* 312 (5778), 1375–1378. <https://doi.org/10.1126/science.1125261> (80-).
- Fernald, F.G., 1984. Analysis of atmospheric lidar observations: some comments. *Appl. Opt.* 23, 652–653.
- Fischer, E., Jones, G., 2012. Atmospheric dimethylsulphide production from corals in the great barrier reef and links to solar radiation, climate and coral bleaching. *Biogeochemistry* 110, 31–46.
- Flamant, C., Pelon, J., Flamant, P., Durand, P., 1997. Lidar detection of the entrainment zone thickness at the top of the unstable marine atmospheric boundary layer. *Bound.-Layer Meteorol.* 83, 247–284.
- Franke, K., Ansmann, A., Müller, D., Althausen, D., Venkataraman, C., Reddy, M.S., Wagner, F., Scheele, R., 2003. Optical properties of the indo-Asian haze layer over the tropical Indian Ocean. *J. Geophys. Res.* 108 (D2), 4059. <https://doi.org/10.1029/2002JD002473>IPCC.
- Garratt, J.R., 1992. *The Atmospheric Boundary Layer*. Cambridge University Press, Cambridge.
- Griffith, W.T.D., 1996. Synthetic calibration and quantitative analysis of gas-phase FTIR spectra. *Appl. Spectrosc.* 50, 59–70.
- Griffith, W.T.D., Deutscher, N.M., Caldwell, C., Kettlewell, G., Riggenbach, M., Hammer, S., 2012. A Fourier transform infrared trace gas and isotope analyser for atmospheric applications. *Atmos. Meas. Tech.* 5, 2481–2498.
- Guérette, E.A., Paton-Walsh, C., Kubistin, D., Humphries, R., Bhujel, M., Buchholz, R.R., Chambers, S., Cheng, M., Davy, P., Dominick, D., Galbally, I., Griffith, D.W.T., Griffiths, A., Keywood, M., Lawson, S., Molloy, S., Selleck, P., Simmons, J., Wilson, S.R., 2017. Measurements of urban, marine and biogenic air (MUMBA): characterisation of trace gases and aerosol at the urban, marine and biogenic interface in summer in Wollongong, Australia. <https://doi.pangaea.de/10.1594/PANGAEA.871982>.
- Jones, G., Curran, M., Broadbent, A., King, S., Fischer, E., Jones, R., 2007. Factors affecting the cycling of dimethylsulfide and dimethylsulfoniopropionate in coral reef waters of the great barrier reef. *Environ. Chem.* 4, 310–322.
- Kaufman, Y.J., Tanre, D., Boucher, O., 2002. A satellite view of aerosols in the climate system. *Nature* 419, 215–223.
- Keywood, M., Kanakidou, M., Stohl, A., Dentener, F., Grassi, G., Meyer, C., Torseth, K., Edwards, D., Thompson, A.M., Lohmann, U., 2013. Fire in the air: biomass burning impacts in a changing climate. *Crit. Rev. Environ. Sci. Technol.* 43, 40–83.
- Kovalev, V.A., 1995. Sensitivity of the lidar solution to errors of the aerosol backscatter-to-extinction ratio: influence of a monotonic change in the aerosol extinction coefficient. *Appl. Opt.* 34 (18), 3457–3462.
- Krogsaeter, O., Reuder, J., Hauge, G., 2011. WRF and the Marine Planetary Boundary Layer. EWEA, Brussels, Belgium, pp. 1–6.
- Lamarque, J.F., Bond, T.C., Eyring, V., Granier, C., Heil, A., Klimont, Z., Lee, D., Liousse, C., Mieville, A., Owen, B., Schultz, M.G., Shindell, D., Smith, S.J., Stehfest, E., Van Aardenne, J., Cooper, O.R., Kainuma, M., Mahowald, N., McConnell, J.R., Naik, V., Riahi, K., Vuuren, D.P., 2010. Historical (1850–2000) gridded anthropogenic and biomass burning emissions of reactive gases and aerosols: methodology and application. *Atmos. Chem. Phys.* 10, 7017–7039. <https://doi.org/10.5194/acp-10-7017-2010>.
- Lammert, A., Bösenberg, J., 2006. Determination of the convective boundary-layer height with laser remote sensing. *Bound.-Layer Meteorol.* 119 (1), 159–170.
- Leahy, S.M., Kingsford, M.J., Steinberg, C.R., 2013. Do clouds save the great barrier reef? Satellite imagery elucidates the cloud-SST relationship at the local scale. *PLoS One* 8, e70400.
- Luo, T., Yuan, R., Wang, Z., 2014. Lidar-based remote sensing of atmospheric boundary layer height over land and ocean. *Atmos. Meas. Tech.* 7, 173–182.
- Mallet, M. D., Desservettaz, M. J., Miljevic, B., Milic, A., Ristovski, Z. D., Alroe, J., Cravigan, L. T., Jayaratne, E. R., Paton-Walsh, C., Griffith, D.W. T., Wilson, S. R., Kettlewell, G., Marcel V. van der Schoot, Selleck, P., Reisen, F., Lawson, S. J., Ward, J., Hamwell, J., Cheng, M., Gillet, R. W., Molloy, S. B., Howard, D., Nelson, P. F., Morrison, A. L., Edwards, G. C., Williams, A. G., Chambers, S. D., Werczynski, S., Williams, L. R., Winton, V. H. L., Atkinson, B., Wang, X. Y., and Keywood, M. D.: Biomass burning emissions in North Australia during the early dry season: an overview of the 2014 SAFIRED campaign, *Atmos. Chem. Phys.*, 17, 13681–13697, 2017.
- McGowan, H.A., Clark, A., 2008. A vertical profile of PM10 dust concentrations measured during a regional dust event identified by MODIS Terra, western Queensland, Australia. *J. Geophys. Res. Atmos.* 113, F02S03. <https://doi.org/10.1029/2007JF000765>.
- Melas, D., Ziomas, I., Zerefos, C., 1995. Boundary layer dynamics in an urban coastal environment under sea breeze conditions. *Atmos. Environ.* 29, 3605–3617.
- Milic, A., Mallet, M.D., Cravigan, L.T., Alroe, J., Ristovski, Z.D., Selleck, P., Lawson, S.J., Ward, J., Desservettaz, M.J., Paton-Walsh, C., Williams, L.R., Keywood, M.D., Mijevic, B., 2017. Biomass burning and biogenic aerosols in northern Australia during the SAFIRED campaign. *Atmos. Chem. Phys.* 17 (6), 3945–3961.
- Mitchell, R., Forgan, B., Campbell, S., Qin, Y., 2013. The climatology of Australia tropical aerosol: evidence for regional correlation. *Geophys. Res. Lett.* 40, 2384–2389.
- Myhre, G., Hoyle, C.R., Berglen, T.F., Johnson, B.T., Haywood, J.M., 2008. Modeling of the solar radiative impact of biomass burning aerosols during the dust and biomass-burning experiment (DABEX). *J. Geophys. Res.* 113, D00C16. <https://doi.org/10.1029/2008JD009857>.
- NOAA, NASA, USAF, 1976. *US Standard Atmosphere 1976*. US Government Printing Office, Washington DC.
- O'Dowd, C.D., Hämeri, K., Mäkelä, J., Väkeva, M., Aalto, P., de Leeuw, G., Kunz, G.J., Becker, E., Hansson, H.C., Allen, A.G., Harrison, R.M., Berresheim, H., Kleefeld, C., Geever, M., Jennings, S.G., Markku, K., 2002. Coastal new particle formation: environmental conditions and aerosol physicochemical characteristics during nucleation bursts. *J. Geophys. Res. Atmos.* 107.
- Paton-Walsh, C., Guérette, E., Kubistin, D., Humphries, R., Wilson, S.R., Dominick, D., Galbally, I., Buchholz, R., Bhujel, M., Chambers, S., Cheng, M., Cope, M., Davy, P., Emmerson, K., Griffith, D.W.T., Griffiths, A., Keywood, M., Lawson, S., Molloy, S., Rea, G., Selleck, P., Shi, X., Simmons, J., Velasco, V., 2017. The MUMBA campaign: measurements of urban, marine and biogenic air. *Earth Syst. Sci. Data* 9 (1), 349–362.
- Pichelli, E., Ferretti, R., Cacciani, M., Siani, A.M., Ciardini, V., Iorio, T.D., 2014. The role of urban boundary layer investigated with high-resolution models and ground-based observations in Rome area: a step towards understanding parameterization potentialities. *Atmos. Meas. Tech.* 7 (1), 315–322.
- Prijith, S.S., Aloysius, M., Mohan, M., 2014. Relationship between wind speed and sea salt aerosol production: a new approach. *J. Atmos. Sol. Terr. Phys.* 108, 34e40.
- Prospero, J.M., Ginoux, P., Torres, O., Nicholson, S.E., Gill, T.E., 2002. Environmental characterization of global sources of atmospheric soil dust identified with the Nimbus 7 total ozone mapping spectrometer (TOMS) absorbing aerosol product. *Rev. Geophys.* 40 (1), 1002. <https://doi.org/10.1029/2000RG000095>.
- Qin, Y., Mitchell, R.M., 2009. Characterisation of episodic aerosol types over the Australian continent. *Atmos. Chem. Phys.* 9, 1943–1956.
- Quinn, P.K., Coffman, D.J., Bates, T.S., Welton, E.J., Covert, D.S., Miller, T.L., Johnson, J.E., Maria, S., Russell, L., Arimoto, R., Carrico, C.M., Rood, M.J., Anderson, J., 2004. Aerosol optical properties measured on board the Ronald H. Brown during ACE-Asia as a function of aerosol chemical composition and source region. *J. Geophys. Res.* 109, D19S01. <https://doi.org/10.1029/2003JD004010>.
- Radhi, M., Box, M.A., Box, G.P., Gupta, P., Christopher, S.A., 2009. Evolution of the optical properties of biomass-burning aerosol during the 2003 southeast Australian bushfires. *Appl. Opt.* 48 (9), 1764–1773.
- Radhi, M., Box, M.A., Box, G.P., Mitchell, R.M., 2012. Biomass-burning aerosol over northern Australia. *Aust. Meteorol. Oceanogr. J.* 62, 25–33.
- Ramanathan, V., Crutzen, P.J., Kiehl, J.T., Rosenfeld, D., 2001. Atmosphere: aerosols, climate, and the hydrological cycle. *Science* 294, 2119–2124.

- Ribeiro, F.N.D., de Oliveira, A.P., Soares, J., de Miranda, R.M., Barlage, M., Chen, F., 2018. Effect of sea breeze propagation on the urban boundary layer of the metropolitan region of Sao Paulo, Brazil. *Atmos. Res.* 214, 174–188.
- Rolph, G.D., Ngan, F., Draxler, R.R., 2014. Modeling the fallout from stabilized nuclear clouds using the HYSPLIT atmospheric dispersion model. *J. Environ. Radioact.* 136, 41–55. <https://doi.org/10.1016/j.jenvrad.2014.05.006>.
- Rosen, J., Young, S., Laby, J., Kjome, N., Gras, J., 2000. Springtime aerosol layers in the free troposphere over Australia: Mildura aerosol tropospheric experiment (MATE 98). *J. Geophys. Res.* 105 (D14), 17833–17842.
- Russell-Smith, J., Yates, C.P., Whitehead, P.J., Smith, R., Cragi, R., Allan, G.E., Thackway, R., Frakes, I., Cridland, S., Meyer, M.C., Gill, A., 2007. Bushfires “down under”: patterns and implications of contemporary Australia landscape burning. *Int. J. Wildland Fire* 16, 361–377.
- Stull, R.B., 1988. *An Introduction to Boundary Layer Meteorology*. Kluwer Academic Publishers.
- Swan, H.B., Crough, R.W., Vaattovaara, P., Jones, G.B., Deschaseaux, E.S.M., Eyre, B.D., Miljevic, B., Ristovski, Z.D., 2016. Dimethyl sulfide and other biogenic volatile organic compound emissions from branching coral and reef seawater: potential sources of secondary aerosol over the Great Barrier Reef. *J. Atmos. Chem.* <https://doi.org/10.1007/s10874-016-9327-7>.
- Takegawa, N., Kondo, Y., Koike, M., Ko, M., Kita, K., Blake, D.R., Nishi, N., Hu, W., Liley, J.B., Kawakami, S., Shirai, T., Miyazaki, Y., Ikeda, H., Russel-Smith, J., Ogawa, T., 2003. Removal of NO<sub>x</sub> and NO<sub>y</sub> in biomass burning plumes in the boundary layer over northern Australia. *J. Geophys. Res.* 108 (D10), 4308. <https://doi.org/10.1029/2002JD002505>.
- Tomasi, F.D., Miglietta, M.M., Perrone, M.R., 2011. The growth of the planetary boundary layer at a coastal site: a case study. *Bound.-Layer Meteorol.* 139, 521–541.
- Tsutsumi, Y., Sawa, Y., Makino, Y., 1999. Aircraft measurements of ozone, NO<sub>x</sub>, CO, and aerosol concentrations in biomass burning smoke over Indonesia and Australia in October 1997: depleted ozone layer at low altitude over Indonesia. *J. Geophys. Res.* 26 (5), 595–598.
- Wang, K.C., Dickinson, R.E., Su, L., Trenberth, K.E., 2012. Contrasting trends of mass and optical properties of aerosols over the Northern Hemisphere from 1992 to 2011. *Atmos. Chem. Phys.* 12, 9387–9398. <https://doi.org/10.5194/acp-12-9387-2012>.
- Winning Jr., T.E., Chen, Y.L., Xie, F.Q., 2017. Estimation of the marine boundary layer height over the central North Pacific using GPS radio occultation. *Atmos. Res.* 183, 362–370.